IOP Publishing Phys. Med. Biol. 65 (2020) 025002 (10pp) https://doi.org/10.1088/1361-6560/ab6178

Physics in Medicine & Biology

IPEM Institute of Physics and Engineering in Medicine

PAPER

Modelling of the focal spot intensity distribution and the off-focal spot radiation in kilovoltage x-ray tubes for imaging

Brent van der Heyden[1], Gabriel Paiva Fonseca[1], Mark Podesta[1], Ivan Messner[2,3], Niklas Reisz[3], Ana Vaniqui[1], Heinz Deutschmann[2], Phil Steininger[2,3] and Frank Verhaegen[1,4]

[1] Department of Radiation Oncology (MAASTRO), GROW—School for Oncology and Developmental Biology, Maastricht University Medical Centre, Maastricht, The Netherlands
[2] medPhoton GmbH, Karolingerstraße 16, 5020 Salzburg, Austria
[3] Institute for Research and Development on Advanced Radiation Technologies (radART), Paracelsus Medical University, Strubergaße 21, 5020 Salzburg, Austria
[4] Author to whom any correspondence should be addressed.

E-mail: frank.verhaegen@maastro.nl

RECEIVED
5 October 2019

REVISED
20 November 2019

ACCEPTED FOR PUBLICATION
13 December 2019

PUBLISHED
16 January 2020

Keywords: x-ray tube, focal spot, off-focal radiation, Monte Carlo, Geant4, cone-beam CT

Supplementary material for this article is available online

Abstract

X-ray tubes for medical applications typically generate x-rays by accelerating electrons, emitted from a cathode, with an interelectrode electric field, towards an anode target. X-rays are not emitted from one point, but from an irregularly shaped area on the anode, the focal spot. Focal spot intensity distributions and off-focal radiation negatively affect the imaging spatial resolution and broadens the beam penumbra. In this study, a Monte Carlo simulation model of an x-ray tube was developed to evaluate the spectral and spatial characteristics of off-focal radiation for multiple photon energies. Slit camera measurements were used to determine the horizontal and vertical intensity profiles of the small and the large focal spot of a diagnostic x-ray tube. First, electron beamlet weighting factors were obtained via an iterative optimization method to represent both focal spot sizes. These weighting factors were then used to extract off-focal spot radiation characteristics for the small and large focal spot sizes at 80, 100, and 120 kV. Finally, 120 kV simulations of a steel sphere ($d = 4$ mm) were performed to investigate image blurring with a point source, the small focal spot, and the large focal spot. The magnitude of off-focal radiation strongly depends on the anode size and the electric field coverage, and only minimally on the tube potential and the primary focal spot size. In conclusion, an x-ray tube Monte Carlo simulation model was developed to simulate focal spot intensity distributions and to evaluate off-focal radiation characteristics at several energies. This model can be further employed to investigate focal spot correction methods and to improve cone-beam CT image quality.

1. Introduction

Diagnostic x-ray tubes are widely used for patient imaging in radiology and radiotherapy. In an x-ray tube, the primary electron beam, emitted from the cathode is accelerated by an interelectrode electric field and focused towards an anode target consisting of a high atomic number material such as molybdenum ($Z = 42$) or tungsten ($Z = 74$). The primary electron beam interacts with the target and produce photons by the deceleration of the electrons (i.e. Bremsstrahlung) or by characteristic x-rays (Verhaegen *et al* 1999). Although photon emission is often assumed to originate from one single point source in computed tomography (CT) image reconstructions, this is a practical approximation and not strictly true. Photons are emitted from a small area on the surface of the anode, which is called the focal spot. Diagnostic x-ray tubes are commercially available with focal spot sizes typically ranging from 0.1 mm to 2.0 mm. A larger focal spot size negatively affects the spatial resolution of imaging and induces a wider x-ray beam penumbra (Law 1993, Ouandji *et al* 2002, Chen *et al* 2008).

After the first interaction round of the primary electron beam on the target anode, a fraction of the electron beam scatters (Kim *et al* 2015) back into the x-ray tube vacuum envelope and, in the presence of the interelectrode electric field, can be redirected back towards the target for a second round of interactions and can generate additional photon radiation. Electrons can backscatter multiple times, yielding multiple generations of decreasing backscatter. A fraction of the re-entry electrons generates photons mostly outside the primary focal spot resulting in the so-called off-focal spot radiation. Off-focal spot radiation is also known as extra-focal radiation (Birch 1976, Bootsma *et al* 2018) or off-focus radiation (Thoræus 1937, Roeck *et al* 1992) and its contribution cannot be neglected in x-ray tubes suitable for diagnostic imaging, as has long been indicated in the literature (Birch 1976). More recently, studies investigated the spectral characteristics of off-focal spot radiation in diagnostic x-ray tubes (Ali and Rogers 2008) and simulated the secondary radiation produced in transmission-type x-ray tubes (Boone *et al* 2012).

The off-focal characteristics of x-ray spectra (position, energy, backscatter generation) are unmeasurable inside the vacuum envelope of the x-ray tube and are often ignored in x-ray tube simulation studies (Verhaegen *et al* 1999, Bazalova and Verhaegen 2007, Jia *et al* 2009, Bontempi *et al* 2010). In faster analytical codes for X-spectrum calculations such as SpekCalc (Poludniowski and Evans 2007, Poludniowski 2007, Poludniowski *et al* 2009) and Spektr (Punnoose *et al* 2016) this effect is also not modelled. Currently there are no standardized methods to measure the off-focal component of x-ray spectra, and so Monte Carlo simulations provide an alternative to obtain these characteristics as simulated particles can be labeled according to their type and interaction history in user-specified categories.

The first goal of this study was to develop a realistic focal spot simulation model in an x-ray tube, and then to quantify the spectral characteristics and the spatial extent of the off-focal radiation due to the influence of the interelectrode electric field. This was investigated for an electron point source at 100 kV and two focal spot sizes at three commonly used diagnostic energies: 80, 100, and 120 kV. The effects of the enlarged focal spot size and the off-focal radiation on image quality was also investigated.

2. Materials and methods

2.1. Simulation model

A Monte Carlo simulation model of the ImagingRing system on rails (IRr) (medPhoton GmbH, Salzburg, Austria) was made using the Geant4 (v10.5) simulation toolkit (figure 1) (Agostinelli *et al* 2003). The IRr system is a special type of cone-beam computed tomography (CBCT) scanner that allows non-isocentric CBCT acquisitions using a monobloc system (x-ray tube and generator) and a flat panel detector that rotate independently to optimize the field of view at the detector level. Geometrical and technical specifications of the IRr system and its components were provided by the IRr manufacturer (medPhoton).

The customized monobloc system (HF1 R-23 ORB X20P, IMD Generators, Grassobbio, Italy) consists of a diagnostic x-ray tube with a rotating disk-shaped (mesh volume) tungsten-rhenium target anode (95% W, 5% Re) that has an anode angle of 10° and a diameter of 6.4 cm, an interelectrode distance of ≈1.5 cm, and an inherent tube filtration of 1.3 mm aluminium at the beam exit window. A discretized interelectrode electric field was simulated perpendicular to the anode central axis in discrete and uniform electric field slabs (50 bins), each with their own electric field strength (V/m), over the active area of the anode (figure 2(b)). Due to the anode angle of 10°, the interelectrode distance is different for every modelled field slab. To compensate for this, the nominal electric field strength assigned to each discretized electric field slab (figure 2(b)) is corrected by a factor ranging between 0.87 (E_1) and 1.17 (E_2). Ignoring this variation in electric field strength (V/m) between the slabs would result in x-ray spectra with incorrect maximum energy. To illustrate, this would mean that when an electron is emitted in e.g. E_1 (figure 2(b)), without nominal field strength correction, the maximum energy in the x-ray spectrum will be 13% too high. Due to this correction factor, the electric field slabs closer to the central axis of the anode (E_2 in figure 2(b)) will have a higher electric field strength than the electric field slabs further from the central anode axis (E_1 in figure 2(b)).

Local electric field distortions causing misfocussed electrons and the individual electric field lines ending perpendicular on the target surface are ignored in this simulation model. The spatial extent of the electric field in the *Y*-direction (14 mm) and the *Z*-direction (13 mm) was determined by manual iteration after the focal measurements until the electric field was able to accelerate all electrons from the optimized small and large focal spot cathode emission fluence.

2.2. Focal spot

2.2.1. Focal spot measurements

In contrast to what is often assumed in CBCT reconstructions, the x-rays generated in the x-ray tube are not originating from one single spot at or within the target. Although the manufacturers aim to focus the electron beam towards as small a spot as possible with the electric field, the focal spot still has a finite spatial distribution

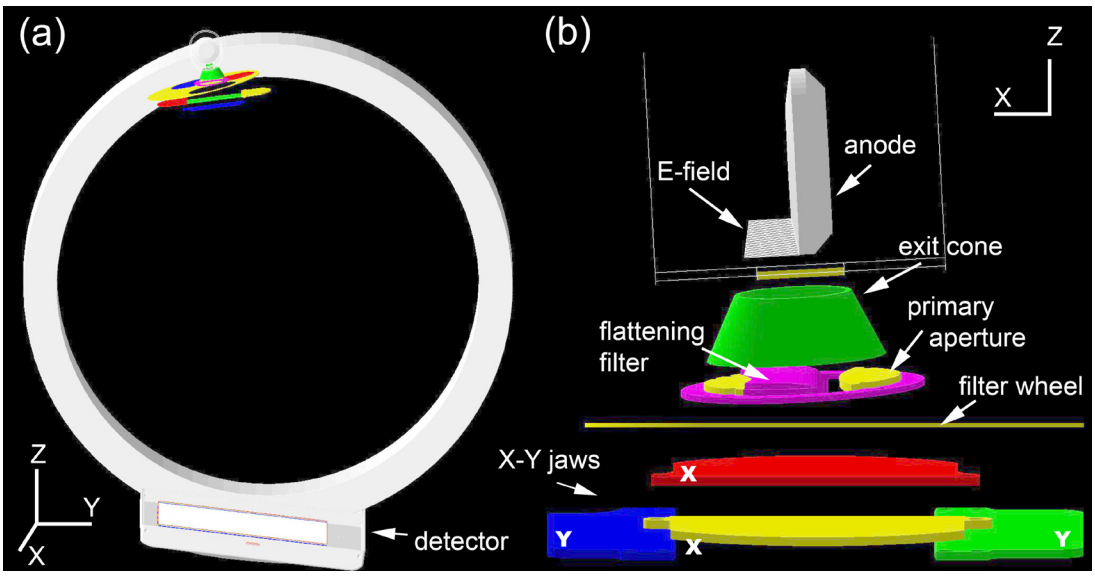

Figure 1. (a) Full Monte Carlo (Geant4) model of the Imaging Ring r (IRr) system and (b) the Monobloc model in more detail.

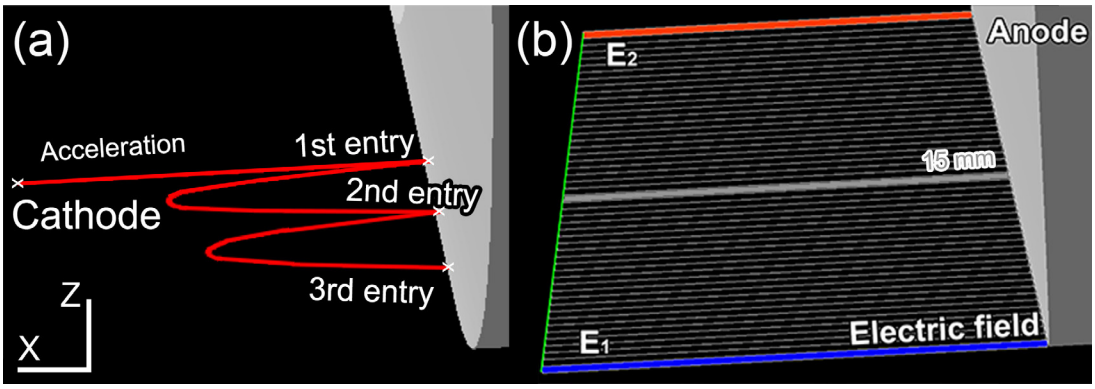

Figure 2. In the left panel (a), a sketch of the backscatter and the generations of re-entry electrons for an accelerated electron between cathode and anode. The interelectrode field between the cathode and the anode is present, but not visualized in this sketch. In this example, the primary emitted electron first hits the target (1st entry), backscatters into the vacuum envelop, bends back towards the anode due to the influence of the electric field (2nd entry), and repeats the same interaction processes until the electron is stopped inside the anode (3rd entry). In the right panel (b), the simulated electric field slabs are visualized between the cathode (green line) and the anode.

which is often not documented. At best, a square or rectangular spot size is quoted which is a first order approximation to the real focal spot intensity distribution. Focal spot measurements are required to have realistic focal spot intensity distributions which can then be used in the Monte Carlo model of the IRr monobloc system. Horizontal and vertical measurement profiles were provided by the manufacturer for the small and the large focal spot, and were acquired with a slit camera (L659117, PTW, Freiburg, Germany) and a XRD 1642 Perkin Elmer flat-panel detector ($40.96 \times 40.96\,cm^2$, $1024 \times 1024\,px^2$) (Rong *et al* 2003). The slit camera consisted of a lead disc with a 0.7 cm opening which was positioned 12.4 cm away from the focal spot.

To reduce noise effects in the next steps of the focal spot shape optimization, the horizontal and vertical profile shapes from the experiment were fitted in 1D to the sum of maximum four normal distributions wherein each distribution was characterized by three parameters: mean, standard deviation, and intensity. Noise effects were reduced to limit the number of beamlets required for the focal spot optimization. After the determination of the fit parameters, a 2D image of the small and large focal spot was obtained by convolving the fitted horizontal and vertical slit camera profiles (figure 3).

Based on the focal spot measurements that showed a non-rectangular distribution and included off-focal radiation, the sizes of the small and the large focal spot were determined in the horizontal and the vertical profiles of the slit experiments at 15% of the maximum intensity to distinguish signal from noise. The small focal spot was 0.66 mm in the horizontal direction and 0.64 mm in the vertical direction, the large focal spot was 0.90 mm in the horizontal and 1.07 mm in the vertical direction.

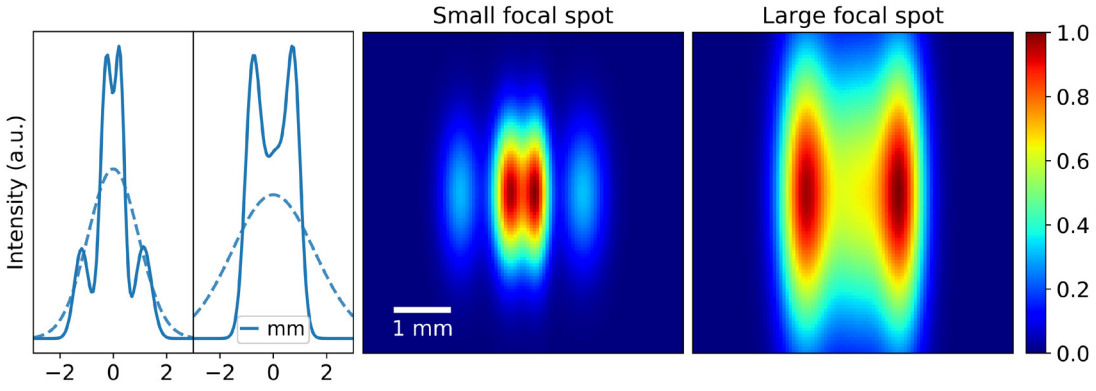

Figure 3. Focal spot slit measurements at the level of the slit camera at 12.4 cm from the focal spot in the horizontal (solid line) and vertical (dashed line) direction through the center of the focal spot for (a) the small focal spot and (b) the large focal spot. The normalized images of the convolved small and large focal spot profiles are shown in (c) and (d).

2.2.2. Focal spot simulations

An optimization model was developed to determine the realistic cathode electron emission fluence in the IRr x-ray tube model, including the simulation of the electric field. In this optimization process, the cathode electron emission fluence was discretized in a regular rectangular grid (green plane in figure 2(b)) with 21 horizontal grid points between −3 mm and +3 mm, and 33 vertical grid points between −8 mm and +8 mm. The boundaries of this rectangular grid were aligned with a $6 \times 6\,mm^2$ imaging beamlet detector that was simulated with a $60 \times 60\,\mu m^2$ resolution at 12.4 cm distance from the focal spot representing the experimental slit camera measurements provided by the IRr manufacturer. Only photons with an incidence angle smaller than 0.3° from the perpendicular x-ray beam axis were detected to mimic the slit camera experiment. A total of 693 (=21 × 33) emitted electron beamlets were simulated with 50×10^6 histories per electron beam and a bremsstrahlung splitting factor of 20 000 as variance reduction technique to reduce calculation time.

After the simulation of the 693 2D electron beamlet projections ($P_{1,\ldots,n}$), their weighting factors ($w_{1,..,n}$) were optimized according to the cost function described by equation (1) to match the convolved 2D distribution of the small and the large focal spot separately (figures 3(c) and (d)). The least-square nonlinear curve-fitting function '*lsqcurvefit*' of the optimization toolbox in MATLAB® R2018b (The MathWorks Inc, Natick, MA) was used to minimize this cost function. During the optimization process, the minimum and maximum value of all weight factors were restricted to 0 and 1, and as constraint the sum of all weight factors must be equal to 1.

$$FS_{conv} = w_1 \cdot P_1 + w_2 \cdot P_2 + .. + w_n \cdot P_n \tag{1}$$

2.3. Electron backscatter simulations

A class was added to the Geant4 simulation to score particle characteristics in the x-ray tube such as the kinetic energy and the interaction position for every particle generation (figure 2(a)). When an electron backscatters for the first time after exiting the target, it belongs to the first generation of backscattered electrons. An electron belongs to the second generation when an electron of the first generation re-enters the target, i.e. it has entered the target three times. The same terminology is applied on subsequent generations.

The derived electron emission fluence distributions of both focal spot sizes were used in the simulations of three different x-ray tube potentials: 80, 100, and 120 kV. Additionally, an electron point source for 100 kV was simulated for comparison (Ali and Rogers 2008). The added Geant4 class also allows for the calculation of the backscatter ratio, re-entry ratio, and bremsstrahlung production. 12.5×10^9 histories were simulated for every tube potential and focal spot combination.

2.4. Steel sphere simulation

A steel sphere ($\rho = 7.7\,g\,cm^{-3}$) of 4 mm diameter was simulated in the IRr model geometry and projections were scored using $0.4 \times 0.4\,mm^2$ resolution using an x-ray tube potential of 120 kV for three source configurations including off-focal spot radiation: (i) one electron beamlet as point source, (ii) the small focal spot, and (iii) the large focal spot. The source-to-object distance was 63.1 cm and the object-to-detector distance was 52.6 cm (IRr specifications). First, horizontal and vertical cross-section profiles through the x-ray projections were evaluated and the full width at half maximum (FWHM) was calculated for each profile. Next, the circular edge spatial frequency (ESF) functions were calculated according to Baer (2003), and then the modulation transfer functions (MTFs) were determined for all source configurations. 5×10^9 million electron histories were

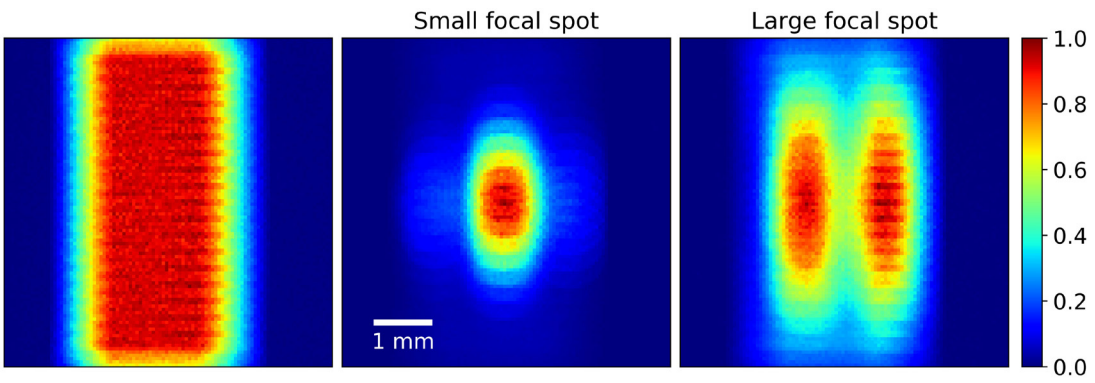

Figure 4. (a) The summed distribution of all individual beamlets before focal spot optimization where all the initial electron beamlets have equal weight. After individual beamlet optimization (equation (1)), the beamlet weights are optimized to obtain the focal spot image of the small focal spot (b) and the large focal spot (c). All panels are normalized to the maximum intensity between 0 and 1.

simulated considering the shape of the source configuration and bremsstrahlung splitting (×20 000) was applied as variance reduction technique.

3. Results

3.1. Focal spot measurements

The horizontal and vertical nominal profiles of the small focal spot (figure 3(a)) and the large focal spot (figure 3(b)) were used to convolve the small focal spot (figure 3(c)) and the large focal spot (figure 3(d)) at the level of the slit camera (12.4 cm from the focal spot).

3.2. Focal spot simulation

From the 693 simulated electron beamlets, 168 beams did not produce a signal at the pinhole camera detector (weight equal to 0) which means that some beamlets in the rectangular electron emission grid points did not produce any signal on the simulated 6 × 6 mm^2 detector. The summed distribution of the individual simulated beamlet grid points that produced a signal is shown in figure 4(a) before optimization. After optimization, the individual beamlets were optimized according to equation (1) to obtain the small focal spot (figure 4(b)) and the large focal spot (figure 4(c)) electron grid point weighting factors which were used in the electron backscatter simulations.

3.3. Electron backscatter simulations

The electron and photon statistics were first determined for a single electron beamlet at 100 kV and then for three different x-ray spectra (80, 100, and 120 kV) for the small and the large focal spot. In table 1, the electron backscatter ratio (in %), report the amount of backscattered electrons from the anode compared to the first entry, and the electron entry ratio (in %) reports the number of re-entering electrons compared to the first entry. The first entry ratio and the 3rd generation bremsstrahlung are not listed in table 1 because the first entry ratio is equal to 100% for all energies and the 3th generation bremsstrahlung was below 0.01%. Most of the re-entry electrons hit the target outside the focal spot. For the small focal spot simulation at 120 kV, only 1.3% of the (9.6%) 2nd entry and 2.1% of the (1.7%) 3rd entry electrons hit the target inside the high focal spot intensity distribution. For the large focal spot at 120 kV, these percentages were equal to 1.4% for the 2nd entry and 2.2% for the 3rd entry electrons. The electron and photon statistics were also simulated for a 20° anode angle instead of a 10° anode angle and are added as supplementary material (stacks.iop.org/PMB/65/025002/mmedia).

Figure 5 presents the calculated energy spectra at all angles for the different generations of backscattered electrons, entry electrons, and produced x-rays inside the x-ray tube target for the small and the large focal spot. The values on the vertical axis indicate the occurrences in every energy bin (in %) relative to the number of 1st entry electrons. The 'fourth generation + ' in the bottom row also contains all higher generations.

In figure 6, the 3D frequency distribution of the entering electrons is visualized. The colormap is normalized to the maximum number of hits in the frequency distribution per generation and only the higher frequency bins are visualized. Therefore, no electron hits are plotted on a large part of the anode surface. The colormap of the frequency distributions in the 2nd and 3rd entry plots of figure 6 are optimized for visualization. Here, the magnitude of the frequency distributions of the 2nd and 3rd entry is ≈5200 and ≈15 800 times smaller than the 1st entry for the small focal spot and is ≈1600 and ≈5000 times smaller than the 1st entry for the large focal spot.

Table 1. Small and large focal spot backscatter, entry, and x-ray production ratios for different generations and three x-ray tube potentials (80, 100, and 120 kV) for a 10° anode angle. The ratios of the simulated beamlet at 100 kV are also listed.

	80 kV		100 kV			120 kV	
	Small	Large	Beamlet	Small	Large	Small	Large
Backscatter ratio (% of the 1st entry)							
1st generation	47.9			48.3		48.4	
2nd generation	6.0	5.8	6.5	6.3	6.0	6.5	6.2
Entry ratio (% of the 1st entry)							
2nd entry	9.0	8.7	9.5	9.3	9.0	9.6	9.2
3rd entry	1.5	1.4	1.6	1.6	1.5	1.7	1.6
X-ray production ratio (% of the 1st entry)							
1st generation	1.11			1.67		2.31	
2nd generation	0.02			0.03		0.05	

The normalized intensity distributions of the focal and off-focal radiation calculated at 120 kV for the small and the large focal spot are depicted in figure 7. The focal distribution has discrete levels due to the primary electron fluence sampling. Summed distributions are calculated for the *Y*-dimension and the *Z*-dimension. In figure 7, the electric field boundaries adopted in this x-ray tube simulation ($H = 1.3$ cm/$W = 1.4$ cm) are indicated by the vertical gray lines. Electrons also re-enter the anode outside the electric field because higher generation electrons are not spatially limited by the simulated electric field. Off-focal radiation can be produced outside the electric field because backscattered electrons were sufficiently deflected by the electric field before escaping the field (negative X-momentum, figure 2).

3.4. Steel sphere simulation

An imaging simulation of a small steel sphere (4 mm diameter) was performed for three different source configurations to evaluate the blurring effect at projection level due to the finite focal spot intensity distributions (figure 8). The FWHMs of the horizontal and vertical cross-profiles were 6.94 and 6.91 mm for the ideal point source, 5.75 and 6.02 mm for the small focal spot, and 4.98 and 5.38 mm for the large focal spot configuration. The circular ESF functions show the steepest curve for the point source simulation and the flattest curve for the large focal spot. The 10% MTF values were 1.82 mm^{-1} for the ideal point source, 0.95 mm^{-1} for the small focal spot, and 0.69 mm^{-1} for the large focal spot.

4. Discussion

In this study, a detailed Geant4 Monte Carlo simulation model was developed to simulate x-ray tube focal spots and evaluate the characteristics of non-focal spot radiation at different generations under the influence of different interelectrode electric field strengths. With the slit camera experiments provided by the manufacturer, the shape of the focal spot was reconstructed, and the electron emission fluence was determined for the small and large focal spot by solving an optimization function iteratively. The simulation model published by Ali and Rogers (2008) was the most advanced model that was available in the literature. In Ali and Rogers (2008), the off-focal component was simulated with an electron point source for different types of x-ray tubes and target materials using a uniform perpendicular electric field; e.g. mammography 26 kV (Mo), diagnostic 100 kV (W), and orthovoltage 250 kV (W) x-ray tubes. The model described in this study is capable to simulate electric emission fluences inside the x-ray tube, e.g. for the small and the large focal spot, and operates at different electric field strengths using an improved electric field simulation model that subdivides the electric field in slabs with corrected electric field strengths. Although only tungsten target materials are investigated, the model described in this study is also configurable for other common target materials and energy ranges such as molybdenum and rhodium in mammography between 22 and 40 kV (Kimme-Smith *et al* 1994, Boone *et al* 1998).

Ali and Rogers (2008) also reported electron backscatter coefficients or ratios (in %) for the diagnostic 100 kV x-ray tube (W) scenario simulated with an electron beamlet. Although backscatter ratios are difficult to compare between target geometries, because of its anode angle dependency, similar first generation backscatter ratios are reported for our diagnostic 100 kV x-ray tube electron beamlet simulation (48.3%) and (Ali and Rogers 2008) (50.6%). Higher generation of backscatter ratios depend on the number of re-entry electrons and thus on the size and strength of the electric field combined with the size of the target anode. The lower generation electron backscatter ratios reported in this study are explained by a smaller electric field size laterally, and smaller target size $H = 1.3$ cm/$W = 1.4$ cm compared to the much larger $H = 2.5$ cm/$W = 10$ cm in Ali and Rogers (2008)

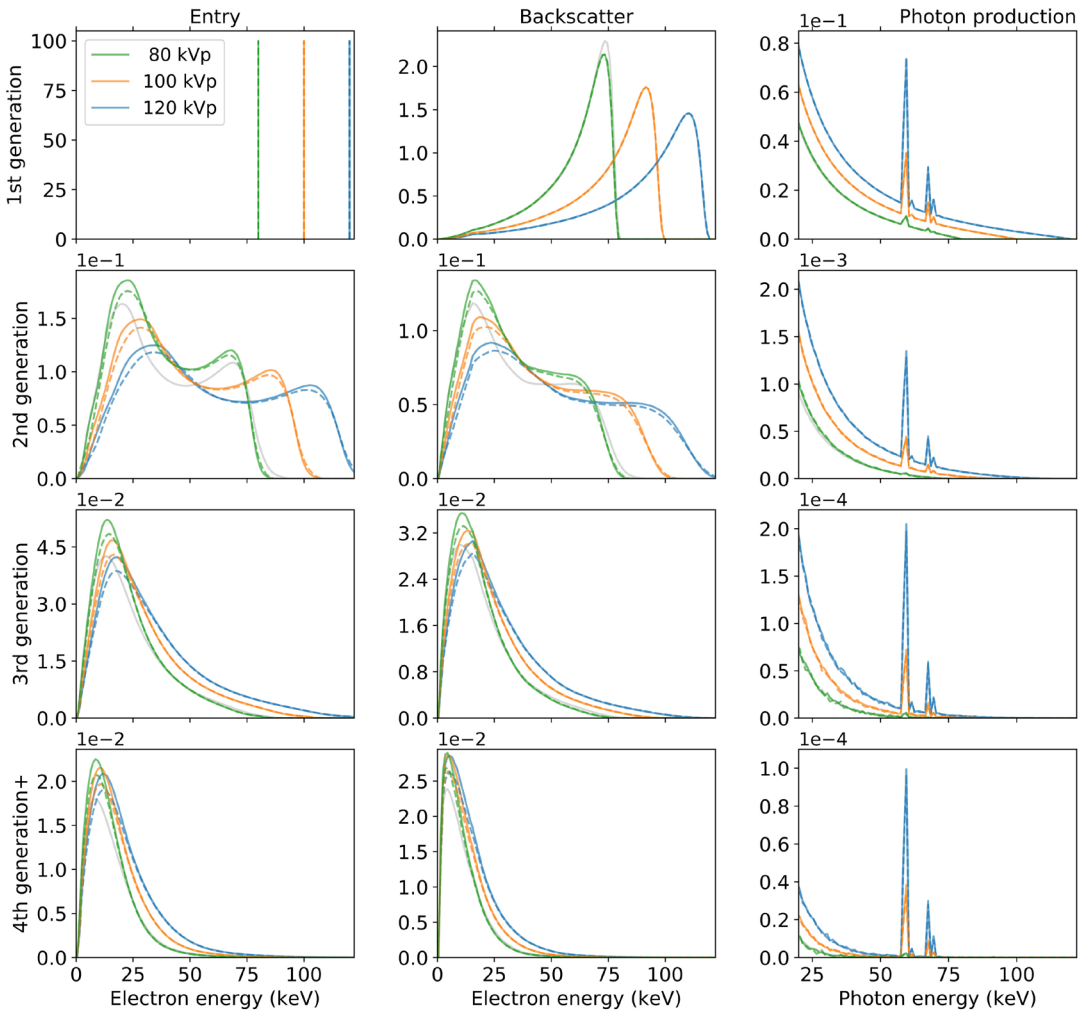

Figure 5. Calculated energy spectra of the entering electrons (left column), backscattered electrons (middle column), and the x-ray production at all angles (right column) on a 10° anode angle for the small focal spot (solid lines) and the large focal spot (dashed lines). The energy spectra of a simulated small focal spot at 80 kV for a 20° anode angle is also plotted as a solid grey line.

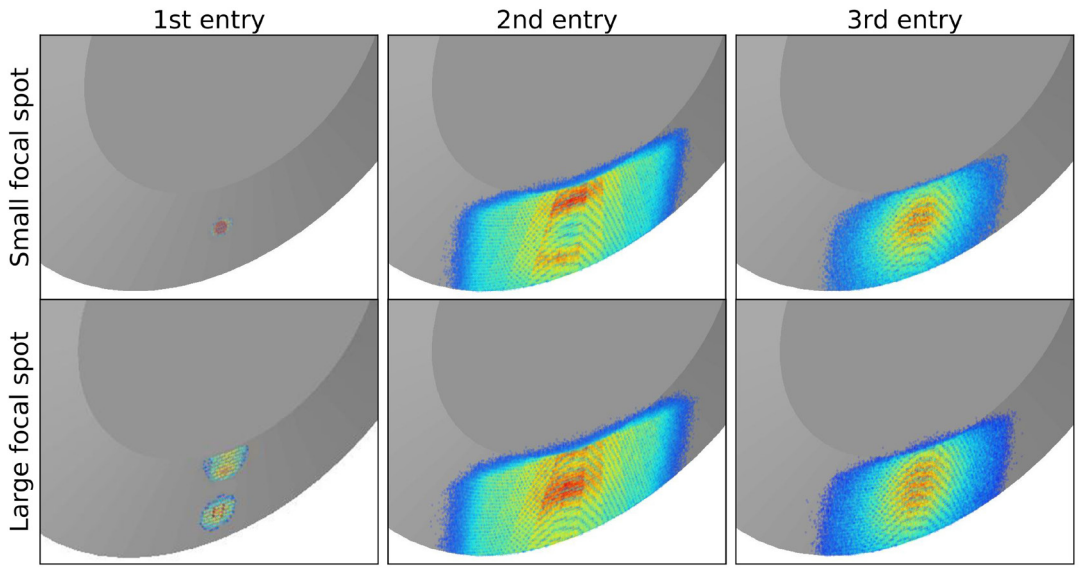

Figure 6. Spatial distribution of the entry electrons for the small (upper row) and the large (bottom row) focal spot for 120 kV. The frequency distribution of each entry generation is normalized to the maximum number of hits per entry.

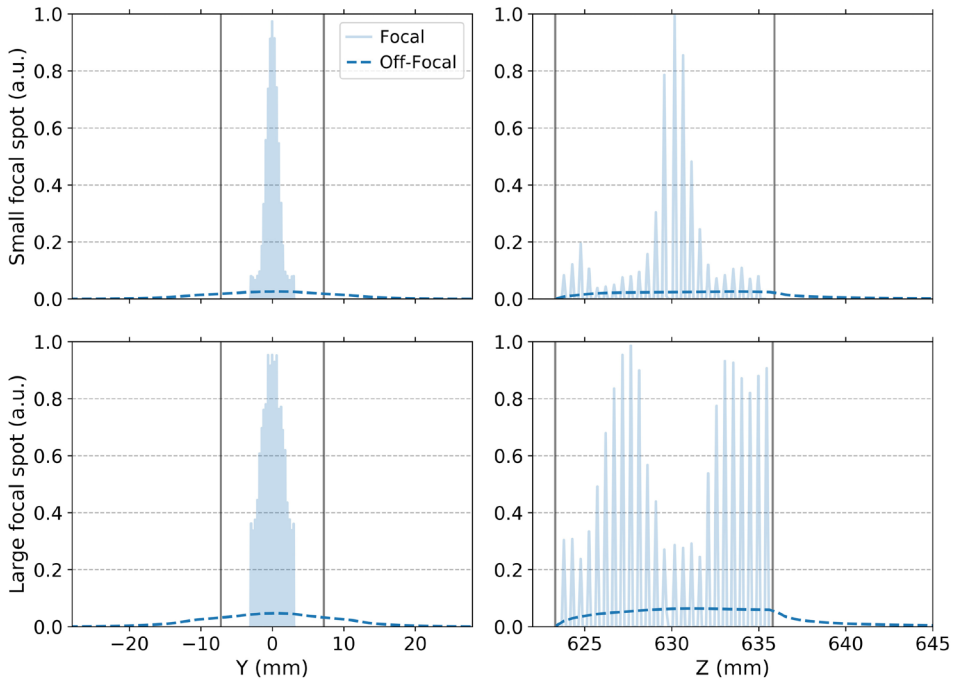

Figure 7. The simulated and summed intensity distribution of the focal (solid) and off-focal (dashed) radiation at 120 kV in the IRr x-ray tube for 1 dimension (*Y* or *Z*, in mm). Intensity distributions are shown for the small (top) and the large (bottom) focal spot. The vertical grey lines indicate the extent of the electric field used in the simulation.

which could be too wide for a realistic diagnostic imaging x-ray tube considering that the electric field forms an electrostatic lens to obtain relatively small focal spot sizes. Smaller targets require a smaller volume wherein the E-field extends, and thus, less electrons will re-enter the target, backscatter again, or produce characteristic x-rays or bremsstrahlung. This is because electrons will exit the electric field lines and will not be bent towards to target again. In the manufacturing process of x-ray tubes, limiting the lateral extent of the electric field will reduce the off-focal radiation component in the imaging beam.

For this x-ray tube setup (i.e. interelectron distance and target size) the effect of the non-focal spot irradiation is limited for diagnostic imaging purposes such as cone beam CT imaging. In the model of a conventional diagnostic 120 kV x-ray spectrum, 2.3% of the primary electrons (1st entry) produces characteristic x-rays or bremsstrahlung and only 0.05% of the primary electrons will produce higher generation x-rays which have a much softer bremsstrahlung spectrum. This increases the probability that the extra-focal spot irradiation will be filtered by either the inherent tube filtration, by the added spectral filters used for diagnostic imaging, or by the x-ray beam collimators (i.e. *X*–*Y* jaws).

The anode angle has a small effect on the backscatter ratios and on the entry ratios listed in table 1 (10°) and as supplementary material (20°). For the 80 kV focal spot simulations, the 1st generation backscatter ratio was 1.5% lower for the 10° anode angle compared to the 20° anode angle. The energy spectrum of the backscattered electrons simulated for a 20° anode angle have a larger high energy peak, which caused a lower 2nd generation entry ratio of approximately 1%, a lower 2nd generation backscatter ratio of 0.5%, and thus a lower 3rd entry ratio of 0.2%. No differences in the x-ray production ratios were observed between the two anode angles because the heel effect affects the x-ray spectrum only after the photon production.

This study focused on the off-focal radiation effect caused by the re-entering of backscattered electrons in the anode material. However, the contaminating extra-focal spot irradiation that softens the x-ray spectrum and broadens the angular distribution of the imaging beam is not only originating from the electron re-entry effect inside the x-ray tube vacuum. Also, Compton and Rayleigh scatter interactions will occur in the anode material, the beam exit window, the additional spectral filtration that absorbs the low energy photons that only contribute to the patient skin dose, and in the imaging beam collimating aperture. Furthermore, backscattered electrons deflected under the influence of the electric field could also produce bremsstrahlung in the x-ray tube shielding made of high *Z* materials. Therefore, the global contribution of extra-focal radiation will be larger than the values reported in this study which are only due the electron re-entering effect on the target.

The focal spot size and its irregular intensity distribution also needs careful investigation for other applications such as precision image-guided animal radiotherapy. Here, collimators with relatively small exit windows, ranging between 0.5 mm and 10 mm, are used to collimate the orthovoltage treatment beam. Especially for the smallest exit windows (≈0.5–1 mm), the beam collimator serves as a pinhole camera and projects the focal spot

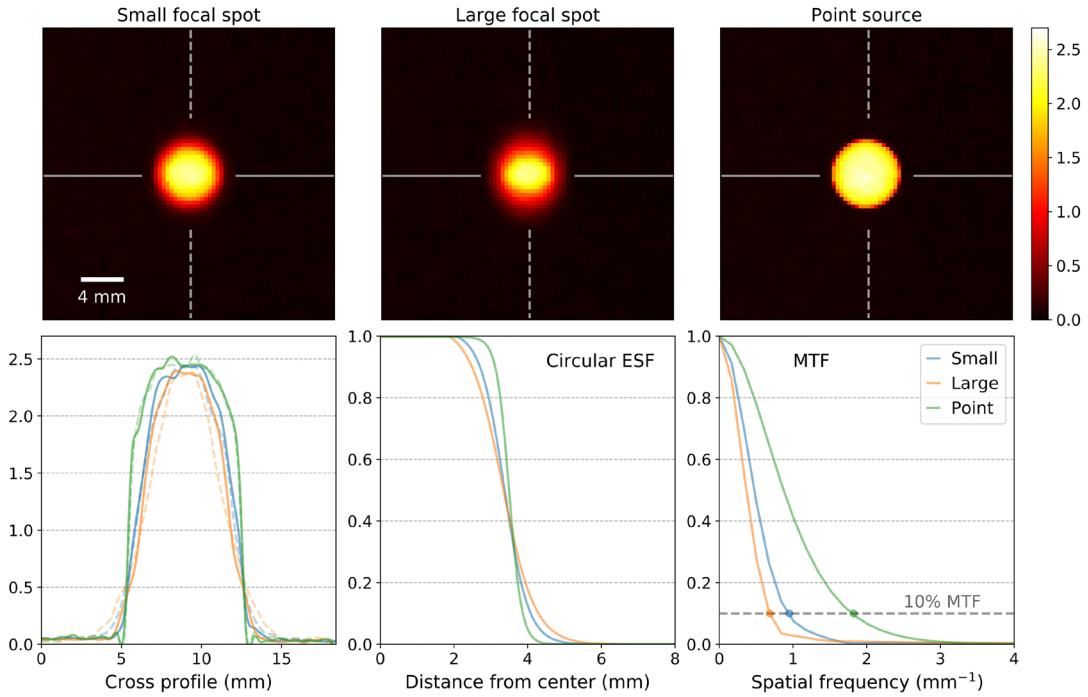

Figure 8. The top row visualizes the simulated projections of a steel sphere with three source configurations at 120 kV for the small focal spot (blue), the large focal spot (orange), and a point source (green). Horizontal (solid) and vertical (dashed) cross profiles were obtained through the image centers indicated by the white crosshair. The bottom row shows both cross profiles, the circular edge spatial frequency (ESF) functions and the modulation transfer functions (MTFs) for all source configurations.

intensity distribution on the animal. Therefore, lacking focal spot intensity models in preclinical radiotherapy limits the accuracy of dose calculations and complicates the modelling of precision irradiation beams and their penumbrae (Granton and Verhaegen 2013, van Hoof *et al* 2019). Exact modelling of focal and off-focal spot could improve the preclinical dose calculations in precision radiotherapy for the smallest beam sizes.

For imaging purposes, efforts should be made, and hardware solutions should be investigated to limit the focal spot size and limit the contribution of extra-focal spot irradiation as these effects lead to an increased imaging beam penumbra and leads to a degraded image quality (figure 8).

In future studies, parameters of this simulation model such as the electric field strength and size, the target material and target mesh volume, and the electron emission fluence can easily be modified to investigate the adverse effects of focal spot distributions and extra-focal spot irradiation in x-ray projection space, or in image space after the (CB)CT reconstruction, and even on the patient CBCT imaging dose (Alaei and Spezi 2015, Ding *et al* 2018) which is of interest when CBCT imaging is used in many fractions over the whole radiotherapy course for example. This model could be used to explore projection-based correction methods for the focal spot induced blurring, such as projection-based deconvolution methods using point-spread functions (Létang and Peix 2003, Nagesh *et al* 2016) or artificial intelligence (Kuntz *et al* 2019).

5. Conclusion

This study described the development of a diagnostic x-ray tube Monte Carlo simulation model which includes the electric emission fluence intensity distribution for two focal spot sizes and the interelectrode electric field to simulate the focal spot intensity distribution and off-focal spot radiation. For our x-ray tube setup for CBCT imaging, the developed simulation model can be used to investigate the adverse effect of (off-)focal spot radiation on image quality.

Conflict of interest

The authors disclosed receipt of joint financial support (Eurostars - MEIRS, reference number 11605; FFG, reference 861339; RVO, Rijksdienst voor Ondernemend Nederland) for the research described in this article.

References

Agostinelli S *et al* 2003 Geant4—a simulation toolkit *Nucl. Instrum. Methods Phys. Res.* A **506** 250–303

Alaei P and Spezi E 2015 Imaging dose from cone beam computed tomography in radiation therapy *Phys. Med.* **31** 647–58
Ali E S and Rogers D W 2008 Quantifying the effect of off-focal radiation on the output of kilovoltage x-ray systems *Med. Phys.* **35** 4149–60
Baer R L 2003 Circular-edge spatial frequency response test *Proc. SPIE* **5294** 524829
Bazalova M and Verhaegen F 2007 Monte Carlo simulation of a computed tomography x-ray tube *Phys. Med. Biol.* **52** 5945–55
Birch R 1976 The spectrum and intensity of extra-focal (off-focus) radiation *Br. J. Radiol.* **49** 951–5
Bontempi M, Andreani L, Rossi P L and Visani A 2010 Monte Carlo simulator of realistic x-ray beam for diagnostic applications *Med. Phys.* **37** 4201–9
Boone J M, Yu T and Seibert A 1998 Mammography spectrum measurement using an x-ray diffraction device *Phys. Med. Biol.* **43** 2569–82
Boone M N, Vlassenbroeck J, Peetermans S, Van Loo D, Dierick M and Van Hoorebeke L 2012 Secondary radiation in transmission-type x-ray tubes: simulation, practical issues and solution in the context of x-ray microtomography *Nucl. Instrum. Methods Phys. Res.* A **661** 7–12
Bootsma G J, Ren L, Zhang H, Jin J Y and Jaffray D A 2018 Monte Carlo analysis of beam blocking grid design parameters: scatter estimation and the importance of electron backscatter *Med. Phys.* **45** 1059–70
Chen L, Shaw C C, Altunbas M C, Lai C J and Liu X 2008 Spatial resolution properties in cone beam CT: a simulation study *Med. Phys.* **35** 724–34
Ding G X *et al* 2018 Image guidance doses delivered during radiotherapy: quantification, management, and reduction: Report of the AAPM Therapy Physics Committee Task Group 180 *Med. Phys.* **45** e84–99
Granton P V and Verhaegen F 2013 On the use of an analytic source model for dose calculations in precision image-guided small animal radiotherapy *Phys. Med. Biol.* **58** 3377–95
Jia P, Xie Y and Bao S 2009 Monte Carlo simulation of x-ray tube spectra with penelope *Congress on Medical Physics and Biomedical Engineering* pp 503–6
Kim S H, Pia M G, Basaglia T, Han M C, Hoff G, Kim C H and Saracco P 2015 Validation Test of Geant4 simulation of electron backscattering *IEEE Trans. Nucl. Sci.* **62** 451–79
Kimme-Smith C, Wang J, DeBruhl N, Basic M and Bassett L W 1994 Mammograms obtained with rhodium versus molybdenum anodes: contrast and dose differences *AJR Am. J. Roentgenol.* **162** 1313–7
Kuntz J, Maier J, Kachelriess M and Sawall S 2019 Focal spot deconvolution using convolutional neural networks *Proc. SPIE* **10948** 109480Q
Law J 1993 The influence of focal spot size on image resolution and test phantom scores in mammography *Br. J. Radiol.* **66** 441–6
Létang J-M and Peix G 2003 On-line x-ray focal spot assessment based on deconvolution using standard imaging devices *NDT & E Int.* **36** 303–17
Nagesh S V S, Rana R, Russ M, Ionita C N, Bednarek D R and Rudin S 2016 Focal spot deblurring for high resolution direct conversion x-ray detectors *Proc. SPIE* **9783** 97833R
Ouandji F, Potter E, Chen W R and Liu H 2002 Impact of focal spot size on the spatial resolution of a digital x-ray imaging system for small animal studies *Biomedical Diagnostic, Guidance, and Surgical-Assist Systems IV* vol 4615
Poludniowski G G 2007 Calculation of x-ray spectra emerging from an x-ray tube. Part II. X-ray production and filtration in x-ray targets *Med. Phys.* **34** 2175–86
Poludniowski G G and Evans P M 2007 Calculation of x-ray spectra emerging from an x-ray tube. Part I. Electron penetration characteristics in x-ray targets *Med. Phys.* **34** 2164–74
Poludniowski G, Landry G, DeBlois F, Evans P M and Verhaegen F 2009 SpekCalc: a program to calculate photon spectra from tungsten anode x-ray tubes *Phys. Med. Biol.* **54** N433–8
Punnoose J, Xu J, Sisniega A, Zbijewski W and Siewerdsen J H 2016 Technical Note: spektr 3.0 A computational tool for x-ray spectrum modeling and analysis *Med. Phys.* **43** 4711–7
Roeck W W, Martin J T and Beach R 1992 Analysis of contributing factors to the occurrence of off-focus radiation (OFR) *Med. Phys.* **19** 1201–4
Rong X J, Krugh K T, Shepard S J and Geiser W R 2003 Measurement of focal spot size with slit camera using computed radiography and flat-panel based digital detectors *Med. Phys.* **30** 1768–75
Thoræus R 1937 The amount of off-focus radiation in beams from various types of roentgen tubes *Acta Radiol.* **18** 753–60
van Hoof S J, Verde J B and Verhaegen F 2019 Dose painting by dynamic irradiation delivery on an image-guided small animal radiotherapy platform *Br. J. Radiol.* **92** 20180744
Verhaegen F, Nahum A E, Van de Putte S and Namito Y 1999 Monte Carlo modelling of radiotherapy kV x-ray units *Phys. Med. Biol.* **44** 1767–89